Alexandria Journal of Science and Technology

Article

Genesis and Geochemical Prospecting Features of Gold Mineralization at the V-Shear Prospect, Gebel El Sukari Gold Mine Area, Eastern Desert, Egypt

Ahmed Hesham Elshayeb [1,2,*], Khalil Isaac Khalil [1], Hossam Ahmed Helba [1]

[1] *Geology Department, Faculty of Science, 21521 Alexandria University.*

[2] *Environmental Studies and Research Institute, University of Sadat City.*

[*] *Correspondence Address:*

Ahmed Hesham Elshayeb: Environmental Studies and Research Institute, University of Sadat City, E.mail address: ahmed.elshayeb@esri.usc.edu.eg.

KEYWORDS: Gold, Eastern Desert, Geochemistry, Orogenic, Prospecting.

Received:
June 10, 2024
Accepted:
July 06, 2024
Published:
August 08, 2024

ABSTRACT: The V-Shear prospect area lies 3 km northeast of the Sukari Porphyry granite. The area occurs within greenschist/amphibolite facies arc metamorphic rocks in association with late tectonic granitic intrusions. The mineralization is confined to quartz veins/veinlets along NE-SW trending shear zones and their associated altered wall rocks. Pyrite and arsenopyrite are the primary hydrothermal sulfide phases, with subordinate pyrrhotite, chalcopyrite, and sphalerite. The main gold budget in the mineralized veins and alteration zones of the investigated gold deposits is recorded within the hydrothermal assemblages. The geological setting, structural elements, mineralogical, and alteration style make features suggestive that the V-Shear prospect belongs to the orogenic gold type. The statistical treatment of two borehole data sets of 494 core samples from the V-Shear area revealed weak enrichment of gold. However, the southeastern borehole contains relatively more Au contents. The R-mode factor analysis of the borehole data sets revealed the existence of five main factors indicating the following associations: (F1) Felsic wallrock association represented by Sn, Be, Zr, Y, and Ba; (F2) Sulfides association represented by Sb, Pb, Mo, Cd, and S; (F3) Mafic wallrock association represented by Ni, Co, Cr, and Li; (F4) Base metal association represented by Cu, Zn, V, and Sr; and (F5) Gold association represented by Au and As. the latter factor has the lowest value of data variability (ca. 8.88%) supporting our finding about the poor gold potentiality in the boreholes. The existence of arsenic among the Au-factor loads suggests using arsenic as a good indicator for gold.

1. INTRODCTION

Gold mineralization has so far been identified and distributed along ~850 km-long extended Pan-African basement of the Eastern Desert of Egypt with more than 100 occurrences. The great majority of gold deposits in Egypt have been classified as epigenetic hydrothermal vein-type and spatially linked to shear zones and quartz veins. The quartz veins are structurally controlled, being fissure filling, confined to fault planes or zones of intensive fracturing [1]. The auriferous veins are commonly surrounded by hydrothermally altered rocks that extend for 1-2m on both sides of the vein [2]. The most important types of wall rock alteration are sericitization, carbonatization, chloritization, silicification, sulfidation, and kaolinitization. Most of gold deposits in Egypt belong to the orogenic vein type [3, 4, 5, 6]. The auriferous veins are almost confined to granitic plutons that intruded metamorphosed ophiolite and/or arc-related rock assemblages [7, 8, 9, 10, 11, 12]. Magmatic and/or metamorphic hydrothermal fluids have been suggested as the transporting fluids, whereas mafic/ultramafic ophiolitic rocks have been postulated as the main source of gold [13, 14, 15, 10, 16, 17, 18, 19, 12].

A lot of studies deal with gold mineralization in the Eastern Desert of Egypt. Most of these studies have been focused on classification, geologic setting, genesis, opaque mineralogy, and alteration. However, very little investigations have been attentive to the geochemical prospecting pattern [20, 21, 22, 23]. In this work, we use recently obtained geochemical data to provide a more detailed characterization of the primary haloes surrounding the undiscovered and unexplored gold resource potential in the V-Shear area of Egypt's Central Eastern Desert.

The V-Shear area is located approximately 3 km northeast of Sukari Porphyry Hill (**Figure 1**) and is considered to be one of the targets generated during the regional exploration along the Sukari tenement.

Alexandria Journal of Science and Technology, 2024, **2**(2), 109–128

Online ISSN: 2974-3273

DOI: 10.21608/ajst.2024.296588.1035

The V-Shear area was not a historical or an old mine, so it was not reported in any previous work. The area was discovered by the exploration team of the Sukari gold mine through surface and subsurface sampling program and divided into V-Shear North, South, and East. Preliminary geologic investigation revealed that the V-Shear North prospect has linkages and similarities to the Sukari Hill, and consequently, it will be the target of the present study.

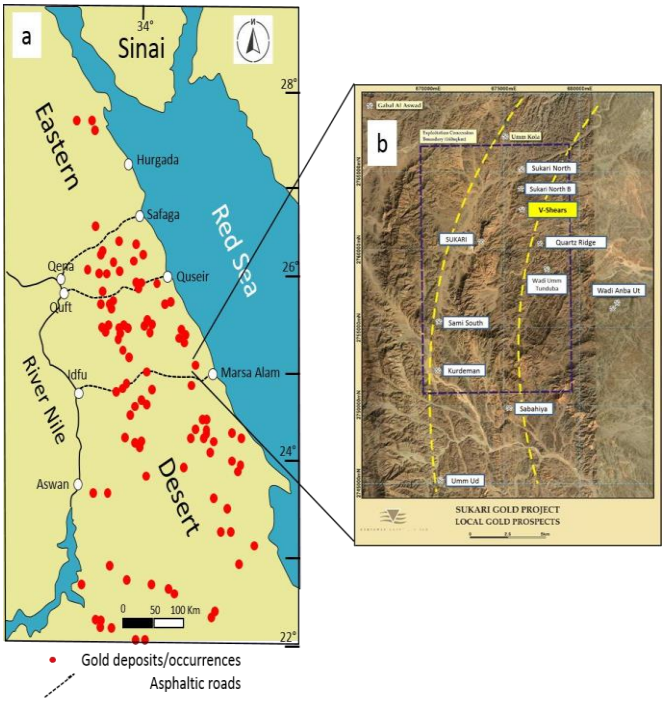

Figure 1. (a) Distribution of gold occurrences in the Eastern Desert of Egypt (El-Ramly et al., 1970); (b) Gold prospects of El Sukari and location of study V-Shear prospect.

2. Geological Setting

2.1 Regional Geology

The Eastern Desert (ED) of Egypt occupies the northwestern part of the Arabian Nubian Shield (ANS) which represents the northern extension of the East African Orogen (EAO) and is dominated by a Neoproterozoic crystalline basement complex (24, 25, 26, 27]. According to absolute ages, prominent differences in exposed lithologies, and remarkable contrast in physiographic features, [28, 29, 30] subdivided the Egyptian Eastern Desert into three main provinces; Northern Eastern Desert (NED), Central Eastern Desert (CED) and Southern Eastern Desert (SED). The NED is characterized by an abundance of post-orogenic felsic granite intrusions, Dokhan volcanics, and molasse-type sediments of the Hammamat Group. The ophiolites form with the arc metavolcanic rocks the main rock units in the CED [31, 32, 33]. Older granitoids are also present and the entire succession of ophiolites, gneisses, metavolcanics, and older granites are occasionally unconformably overlain by Dokhan volcanics and molasse sediments (Hammamat sediments) and intruded by younger pink to red granites. The SED, on the other hand, is characterized by a high proportion of Cryogenian granites and a relatively high abundance of gneisses and migmatites [34, 35, 36].

2.2. Local geology of the V-Shear North area

The V-Shear North area comprises three major lithological domains which are mélange association, metavolcanics, and metagabbro-diorite complex (**Figure 2**). These lithological domains are intruded by small masses of porphyry granites and cut later by very common acidic porphyritic dyke swarms.

The mélange rocks dominate the southern and extreme western parts of the area (**Figure 2**) and are mainly composed of serpentinite and metasediments. The mélange rock units are highly tectonized matrix and include embedded rootless fragments of diorite bodies. The serpentinites are dark greenish-black, weakly to moderately foliate, and intensely altered to produce highly ductile talc-carbonate and highly silicified listvenite. The talc-carbonate rocks are highly foliated, particularly along shear zones. The listvenite is characterized by light green to red colors and usually occurs along the lithological contacts between the mélange rock units and diorite masses (**Figure 3a**). The metasedimentary units are highly ductile foliated and layered rocks (**Figure 3b**). Locally, the metasedimentary rocks are strongly silicified which are highly resistant to deformation (**Figure 3c**). These units have light grey, black to green colors and are composed of moderate- to coarse-grained clastic sediments of variable compositions embedded in a fine-grained matrix.

These metavolcanics are considerably schistosed and the general strike of the schistosity is NNE-SSW with a subvertical dip. The rocks are represented mainly by meta-andesites that occupy ~ 50% of the study area (**Figure 2**). The meta-andesite rocks are characterized by different textures dominated by porphyritic and aphanitic, and less common amygdaloidal. Locally, agglomerates are extended parallel to the schistosity and banding of the meta-andesite

The metagabbro-diorite complex is dominated by metadiorite composition. It exists as elongated scattered bodies and may form larger rigid hills intruding the mélange rocks (**Figure 3d**), especially in the middle and western parts of the V-Shear North prospect. The metadiorite is characterized by a medium to fine-grained phaneritic texture composed mainly of amphiboles and plagioclase. These rocks are generally fractured and exfoliated and weakly to moderately alter along shear zones.

Small granitic intrusions are exposed in the study prospect. The granite masses have sharp intrusive contacts against the surrounding country rocks. These granitic masses have a granodiorite to tonalite composition. The fresh rock is leucocratic, coarse-grained, and pink in color. The dyke swarms are very common in the study area trending ENE to E. They are fine-grained acidic porphyritic dykes of greyish to reddish colors with white plagioclase and quartz phenocrysts.

2.3. Style of Gold Mineralization

Gold mineralization in the V-Shear area is confined to the quartz veins/veinlets and the surrounding alteration zones; both are marked by the presence of shear zones (**Figure 4a**).

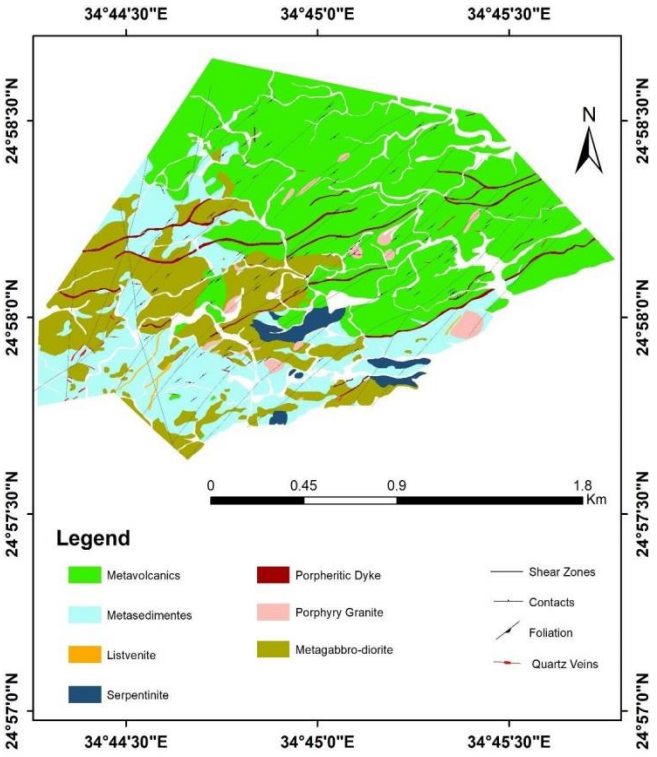

Figure 2. Simplified geologic map of the V-Shear North prospect area (Sukari Gold Mine).

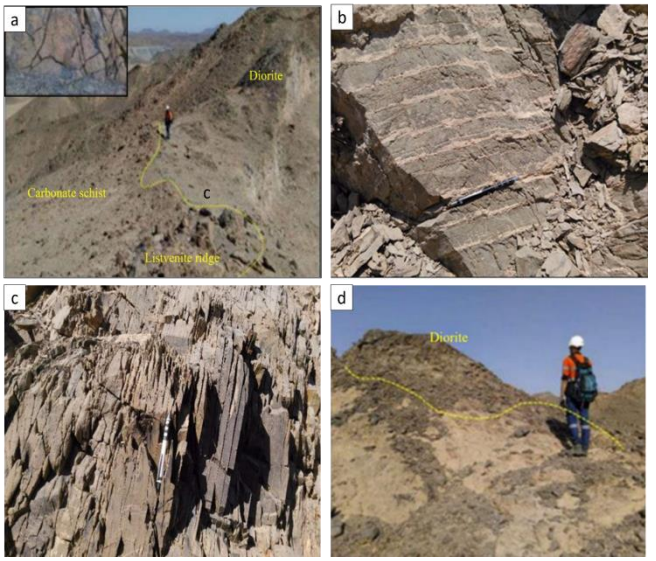

Figure 3. Selected field relations showing: (a) A listvenite ridge rimming the contact between the diorite and carbonate schist (looking NW). (b) Metasediment outcrops showing the sedimentary layering looking (NNW). (c) Highly silicified metasediments exhibit a clear bedding preservation. (d) Diorite rocks intrude on the carbonate schist (looking SW).

Most of the major veins are dipping toward the WNW to NW and trending NE-SW with dip angles ranging from moderate, sub-vertical to vertical exhibiting a dextral sense of movement southeast. The thicknesses of quartz veins range from 0.3 to 0.7 m. Two prospects are explored in the study area. The first prospect is located in the northern part of the area and is related to SE– dipping to sub-vertical narrow shear zones injected by sheared quartz veins and veinlets (**Figure 4b**). This shear zone is localized within the meta-andesites along their contacts with the metadiorite. It comprises carbonate and iron hydroxide minerals (e.g., goethite, limonite) which stained the rock with a red color. The second site, on the other hand, occurs in the south part of the V-Shear prospect. It is mostly confined along the contacts between the highly carbonatized mélange belt and the fractured diorite intrusions (**Figure 4c**). These contacts are often marked by the presence of listvenite dykes.

Figure 4. Field photographs showing: (a) Intense shear zone injected by mineralized quartz veinlets (arrows) and stained by iron hydroxide minerals, north of V-Shear area, (b) Narrow intense shear zone composed of carbonate alteration hosting quartz veins; (c) Minor fault splay in quartz veins and the diorite host rocks.

3. Methodology

About 600 subsurface samples were collected from 7 diamond boreholes drilled in the V-Shear area (**Figure 5**). The boreholes were selected to cover least altered rock types, quartz veins, and alteration types to appropriately accomplish the study's goal. The petrographic features of these rock types were investigated using a total of 36 polished-thin sections.
Geochemical investigations were conducted on all the 600 core samples obtained from the selected diamond drill holes. The preparation and Au measurement procedure were first done by the Sukari Gold Mines site lab and then another copy of pulverized samples to Bureau Veritas Minerals Pty Ltd Lab, Australia for Au and multi-elements. For Au analysis, the El Sukari Gold Mines Site Lab uses Atomic Absorption Spectrometers (Agilent 55BAA and AAS 50B). The limit of detection for Au is <0.01ppm. Two types of standards are used: (i) solution standards for calibration of the AAS

(1000ppm Au standard with matrix 10% HCL and 4% HNO_3), and (ii) solid standards for checking with known value run with the analyzed samples. However, multi-element analysis in Bureau Veritas Minerals Pty Ltd Lab-Australia was performed using the ICP-MS technique (Perkin Elmer Optima 8300 and Thermo Fisher ICAP 6000 series).

Figure 5. (Location map of the V-Shear area with the selected 7 diamond drill holes (VSSD004, VSSD010, VSD019, VSSD020, VSSD022, VSD025, and VSSD026).

For detailed statistical geochemical analysis, 494 core samples from selected two boreholes (VSSD022 and VSD025) were used to shed light on the characters of the primary geochemical haloes and pathfinder elements surrounding and associating the mineralization of the V-Shear area. The two boreholes were chosen based on their rock type and their geographic distribution. Twenty-one elements: Au, As, Sb, Cu, Pb, Zn, Mo, Sn, V, Sr, Ba, Be, Rb, Ni, Li, Cd, Co, Cr, Zr, Y and S were chosen for this study. The raw data of the element concentrations for each borehole were treated by applying univariate and multivariate statistical techniques using SPSS computer software for most calculations, and Strater software for subsurface profiles and mapping. The raw data of element concentrations were transformed to logarithmic values to alleviate their skewness behavior. In univariate analysis histograms and Tukey box-Whesker plots were constructed to study the distribution parameters of the uni-element concentrations. Threshold values were calculated by applying the method of [37] using median and median absolute deviation (MAD) values. For multivariate analysis, principle component R-mode factor analysis was applied. To overcome the closure problem of compositional datasets, we calculated and applied a centered log-ratio (CLR) transformation [38] to the elemental data before factor analysis [39, 40]. Factor loadings with only eigenvalues greater than 1 were extracted, meaning only factors that explain as much variability equivalent to at least one original variable are considered important. The extracted factors were subjected to orthogonal rotation by the Varimax method [41] to maximize the variability among all input variables and, thus, facilitate the interpretation of the factor loadings. To determine which factor loading is significant, the 'broken-stick' method applied by [42] was applied.

4. Petrography

The petrographic study points to that the gold mineralization is confined to the quartz veins and surrounded alteration zones that derived almost from the metavolcanics, and metagabbro-diorite rock units in the V-Shear area.

The metavolcanic rocks at the V-Shear prospect are represented by common meta-andesite and minor meta-rhyodacite. The meta-andesites are porphyritic with abundant plagioclase feldspar (An_{30-35}) and less common hornblende, biotite, and secondary quartz, chlorite, and epidote, whereas apatite and opaques are accessory minerals. The groundmass is mostly composed of plagioclase laths with subordinate biotite and quartz (**Figure 6a**). The meta-rhyodacite, however, comprises plagioclase (An_{30-35}) and quartz phenocrysts embedded in a fine-grained groundmass of quartz, and feldspar (**Figure 6b**). Sericite and calcite are secondary minerals.

The metagabbro-diorite rock type is dominated by dioritic rather than gabbroic composition. The meta-diorite rock is composed essentially of plagioclase feldspar (> 65%) with less common quartz and biotite. Coarse-grained plagioclase feldspar (An_{35-40}) has a tabular to prismatic form with broken twin lamellae embedded in a matrix of relatively fine-grained plagioclase feldspars and quartz (**Figure 6c**). The rock contains traces of chlorite, epidote, calcite, and sericite as secondary minerals. Apatite and opaque magnetite are the main accessories. Opaque oxide minerals such as chromite, ilmenite, and titanomagnetite are disseminated in both the metavolcanic and metagabbro-diorite rock units. Chromite is locally transformed to ferritchromit, whereas ilmenite and titanomagnetite are altered to rutile and anatase. Rutile and anatase are frequently observed along the foliation of the wall rocks and also inherited as inclusions in the sulfides of the altered rocks and quartz veins.

Quartz and quartz-carbonate veins and veinlets are widely distributed in the V-Shear prospect area. Quartz veins display different colors from smoky, grey to milky white. Under the microscope, quartz grains are anhedral with grain sizes ranging from 300 to 900µm along with some measurements up to 4 mm. The quartz crystals are frequently arranged perpendicular to the vein walls showing comb texture (**Figure 6d**). Carbonates, opaque sulfides, sericite, and undigested wall rock materials are the common inclusions in the quartz veins. Quartz grains often exhibit different deformational features such as wavy extinction, deformation lamellae, shearing, and granulation along micro shear zones (**Figure 6e, f**).

The quartz veins are enveloped by haloes of alterations that in part reach up to 10m thick. Sericite/muscovite, carbonate, chlorite, secondary quartz, and sulfides are the most common alteration minerals. Sericite is the most abundant alteration mineral with modal % increases toward the quartz veins. Sericite/muscovite is frequently formed at the expense of feldspars (**Figure 6g**). Alteration of feldspars is either partial or completely forming pseudomorphic texture. Carbonatization is manifested by the formation of calcite which occurs in two forms; (i) polycrystalline rhombic crystals in the form of aggregates or patches, and (ii) veinlets and fracture fillings. Some opaques and quartz could be associated with calcite veinlets (**Figure 6h**). Hydrothermal chlorite is abundant in

most altered samples and is characterized by a flaky form with abnormal blue interference. Chlorite is mostly formed by the replacement of biotite and hornblende (**Figure 6i**).

Most of the studied samples were affected by silicification which led to the formation of secondary quartz and quartz veins and veinlets (**Figure 6d-f**). In the altered wall rocks, secondary quartz is manifested by the presence of cavity fillings in the form of amygdale-like bodies and spherulites of silica. Secondary quartz occurs as monocrystalline to aggregate fine-grained irregular crystals.

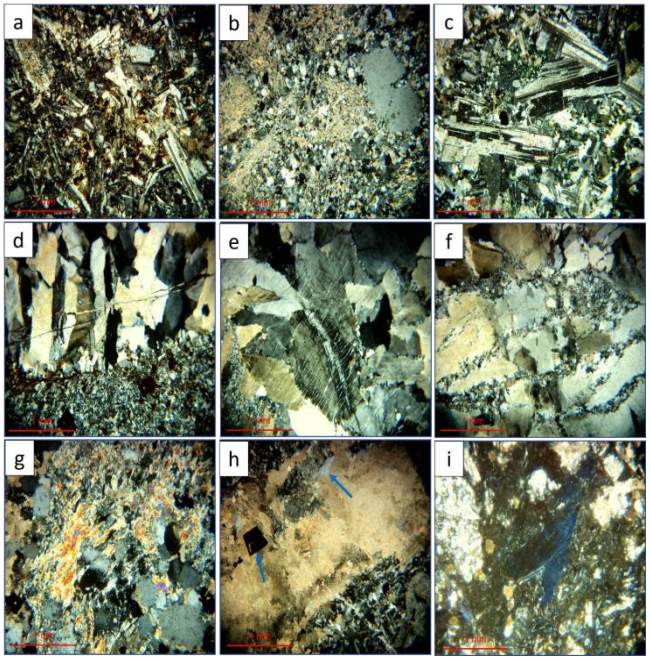

Figure 6. Photomicrographs of the fresh host rocks (a-c), quartz veins (d-f), and altered rocks (g-i) showing: (a) Meta-andesite variety composed of relatively coarse-grained plagioclase embedded in a fine-grained matrix of subhedral plagioclase laths, (XPL); (b) Meta-rhyodacite consists of phenocrysts of plagioclase and quartz crystals embedded in a fine-grained groundmass of quartz, feldspar, and sericite (XPL); (c) Cracked plagioclase crystals with broken twin lamellae filled with chlorite, (XPL); (d) A quartz veinlet, in which quartz grains are aligned perpendicular to the vein walls; (XPL); (e) Deformation lamellae of quartz grains, (XPL); (f) Shearing, and granulation of quartz grains along micro shear zones, (XPL); (g) Plagioclase feldspar crystals are strongly altered to sericite/muscovite (XPL); (h) Calcite veinlet with some opaques (arrow 1) and quartz (arrow 2) inclusions, (XPL); (i) Chlorite with abnormal blue interference colors replaces biotite, (XPL);.

Sulfides are frequently observed in the quartz veins and alteration zones derived from the host metavolcanic and metadiorite rocks. Pyrite and arsenopyrite are the most dominant sulfide minerals. Pyrite constitutes ~50 modal% of the opaque sulfides and displays two forms. Pyrite I usually displays idiomorphic to hypidiomorphic, cubic, and pentagonal crystals with grain sizes commonly < 100 µm (**Figure 7a**), and occurs along the contacts between the quartz veins and wall rock (**Figure 7a**). Pyrite II often occurs as inclusions in the quartz veins with grain sizes up to 2mm. It displays deformed xenomorphic to hypidiomorphic crystals (**Figure 7b**). Arsenopyrite comprises ~40% of opaque sulfides on average. It occurs as disseminated grains, in a distinctive rhombic form that has various sizes from 100 µm up to 1 mm. However, some arsenopyrite grains have corroded contacts against the wall rocks showing a replacement relationship (**Figure 7c**). Coarse-grained arsenopyrite crystals sometimes show deformational texture, and the resulting cracks are filled with native gold (**Figure 7c**). Many inclusions of rutile and wall rock materials are frequently observed in pyrite and arsenopyrite crystals (**Figure 7c & d**).

Chalcopyrite, pyrrhotite, and sphalerite are of minor abundance. Chalcopyrite occurs as very fine discrete or disseminated xenomorphic grains with irregular and corroded crystal outlines in the altered rocks. Pyrrhotite occurs as fine-grained corroded xenomorphic inclusions (≤ 30 µm) in pyrite and arsenopyrite; often associated with fine-grained chalcopyrite (**Figure 7e**). Sphalerite typically occurs as dark grey anhedral crystals intergrown with exsolved chalcopyrite bodies. Visible gold occurs as fracture filling along deformational cracks in pyrite and arsenopyrite as well as quartz veins.

In surface and near-surface samples, most sulfide and oxide ore minerals are oxidized to form goethite and lepidocrocite. Pseudomorphic of goethite and/ or lepidocrocite after pyrite and magnetite are frequently observed. Relicts of sulfide and magnetite minerals are observed in the newly formed goethite/lepidocrocite grains.

5. Geochemistry

5.1. Geochemistry of least altered rock

The chemical analyses of 45 samples representing the least altered rock types from four boreholes in the V-Shear area are given in Table 1. The least altered samples were geochemically identified by using the Ishikawa alteration index (AI = [100(K_2O+MgO) / (K_2O+MgO+CaO+Na_2O)], where samples of AI < 50% are considered as least altered ones [43, 44].

All the investigated rock types are characterized by lower contents of large ion lithophile elements (e.g. Cs, Rb, Ba, and Sr) and high field strength elements (e.g. Th, U, Nb, Ta, Zr, and Hf), and higher contents of P, Co, Cu, Sc, V, W, and Sb than those of the upper continental crust values (**Figure 8**). When plotted on the AFM diagram, the least altered rock types reveal calc-alkaline affinity (**Figure 9a**). On the A/CNK vs. A/NK diagram, the studied meta-diorite samples exhibit a metaluminous nature while the meta-andesite and meta-rhyodacite samples are distributed between the peraluminous and metaluminous fields (**Figure 9b**).

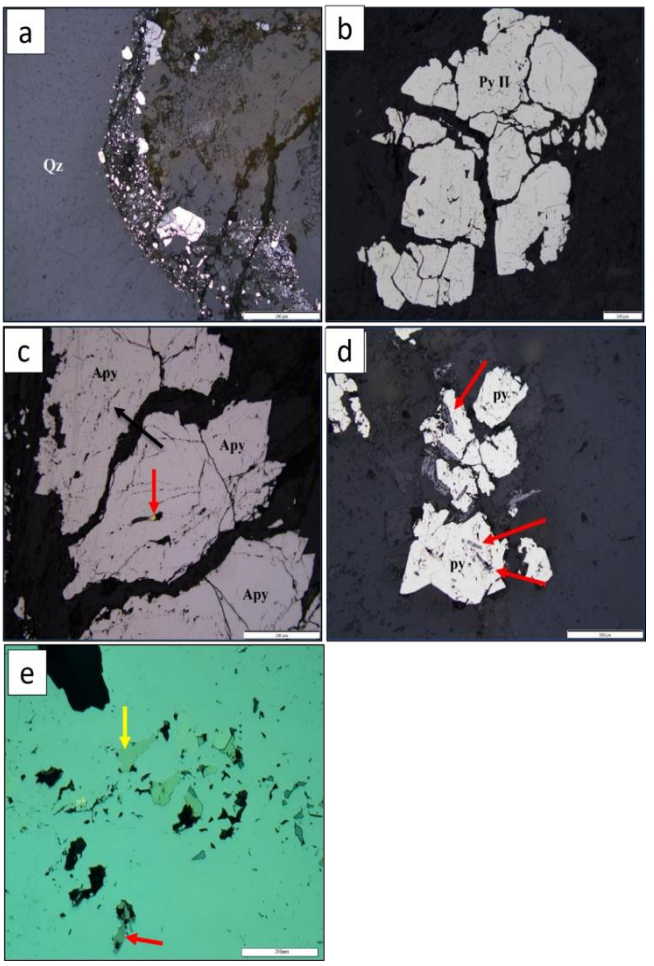

Figure 7. Reflected light photomicrographs of opaque sulfides showing: (a) Pyrite I confined to the wall rock alteration. Note that the quartz vein (Qz) is sulfide-free; (b) Highly deformed crystal of coarse-grained pyrite II (Py II) showing cataclastic texture; (c) Highly deformed arsenopyrite crystals (Apy) with wall rock relics (black arrow) and fracture-filling native gold (red arrow); (d) Needle-like rutile inclusions (red arrows) parallel to the foliation of the pre-existing wall rock in the host pyrite (Py); (e) Relics of pyrrhotite (red arrows) and chalcopyrite (yellow arrow) are observed in pyrite.

The variation of Ba and Rb versus Sr contents in study rock types (**Figure 10a, b**) reveals decreasing Sr contents with a gradual increase in Rb, the behavior consistent with magmatic differentiation. This relation is more pronounced in the meta-andesite samples, less pronounced in the meta-rhyodacite, and poorly exhibited by the meta-diorite samples. However, on the ternary Rb-Ba-Sr diagram all the analyzed samples fall within the high Ba-Sr low differentiation field (**Figure 10c**). On the Rb versus K/Rb plot (**Figure 10d**), a weak negative correlation can be observed for all samples. However, the plot exhibits less contents of incompatible Rb in the meta-diorite samples compared with both meta-andesite and meta-rhyodacite samples. On the other hand, the enrichment of Cu and Zn compared to Pb is illustrated on a ternary diagram of Pb-Cu-Zn, where all samples plot in the high Cu-Zn field (**Figure 10e**).

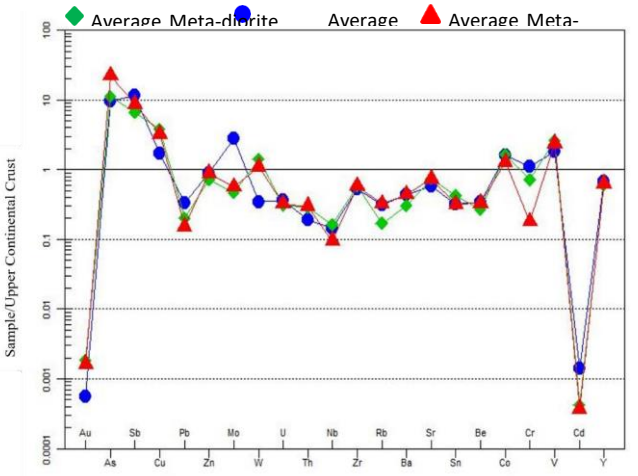

Figure 8. Upper continental crust normalized multi-element patterns for the investigated rock types in the V-Shear study area. Normalization values after [62].

.

The chondrite normalized REE pattern of the investigated rock types exhibits general higher LREE abundances relative to the HREE with a very weak negative Eu anomaly for the meta-diorite and meta-andesite varieties but no Eu anomaly for the meta-rhyodacite variety (**Figure 11**). Average Eu/Eu* ratio of 0.158, 0.149, and 0.156 was recorded for the meta-diorite, meta-andesite, and meta-rhyodacite rock varieties, respectively. The latter variety is characterized by higher average contents of total REE (134.74, Table 1).

According to the tectonic setting discrimination diagrams of [45] and [46], the analyzed samples of the investigated rock types are plotted in the island-arc field (**Figure 12a, b**).

6. Geochemical prospecting

494 analyses of core samples from two representative boreholes in the investigated area were subjected to detailed lithochemical statistical analysis using SPSS software. The chosen boreholes are BH22 (263 samples of 264 m depth) in the western part of the area and BH25 (231 samples of 232 m depth) in the eastern part of the area. The descriptive distribution parameters of 17 selected elements in the chosen boreholes are shown in (Tables 2 and 3). All the datasets of the selected elements exhibit bi- to multi-modal skewed distributions.

6.1. Background and threshold determination

In this study, the background and threshold values were determined as median and median + 2 MAD "median absolute deviation, respectively [37, 40].

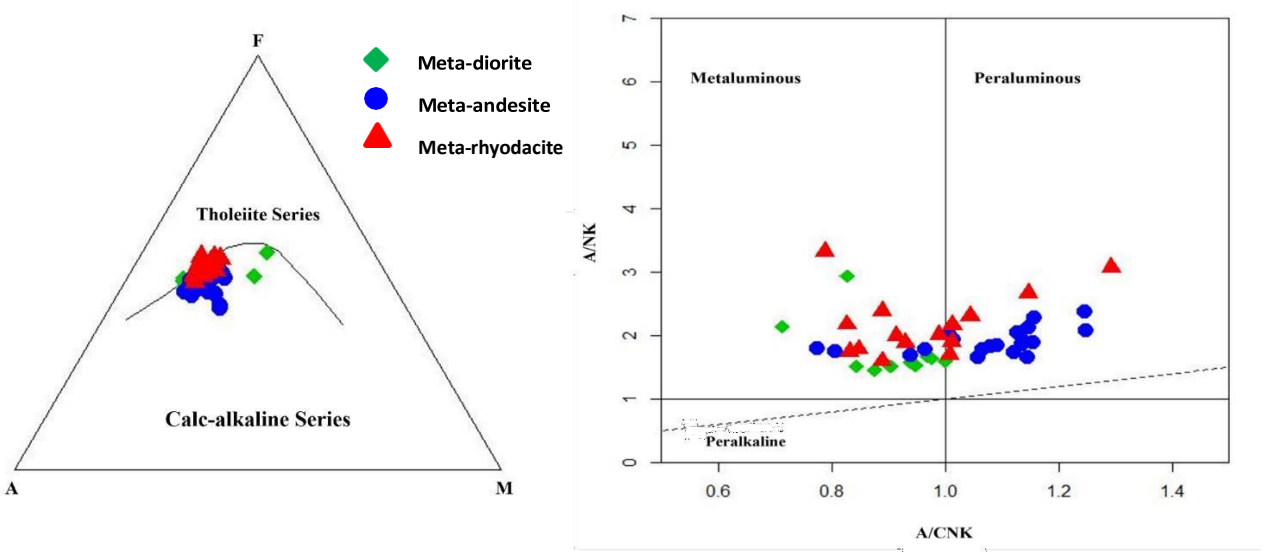

Figure 9. Petrochemical discrimination diagrams for the studied rock types (a) AFM ternary plot after [63], (b) A/CNK vs. A/NK diagram after [64].

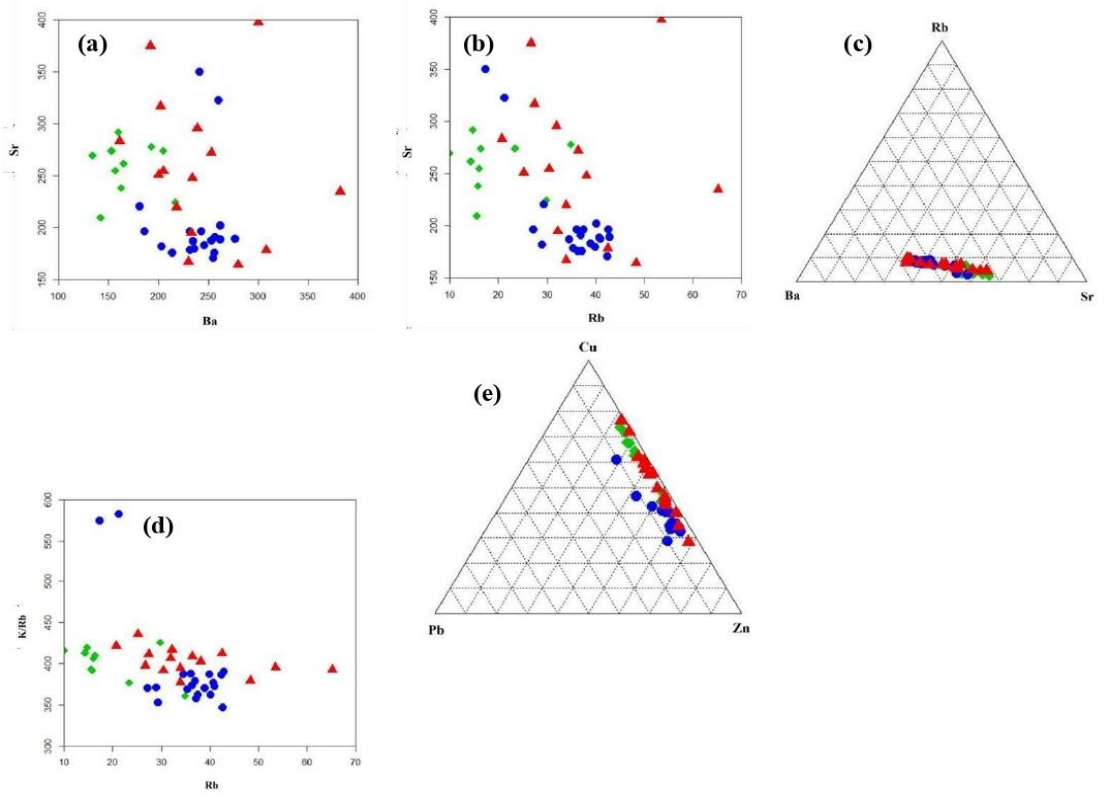

Figure 10. Variation diagrams of (a) Ba vs. Sr, (b) Rb vs. Sr, (c) Ba-Rb-Sr ternary plot, (d) Rb vs. K/Rb, (e) Pb-Cu-Zn ternary plot for the investigated rock types in the V-Shear area. Symbols as in (Figure. 9).

Table 1: Representative chemical analyses of major (wt%), trace, and Rare Earth Elements (ppm) of the least altered rock types in the V-Shear area.

	Meta-diorite (no. of samples = 10)					Meta-andesite (no. of samples = 20)					
Sample No/oxides	307	311	315	318	Average (n=10)	358	360	362	365	Average (n=20)	Clarke values**
TiO2	0.595	0.415	0.404	0.377	0.456	0.548	0.562	0.568	0.609	0.548	0.68
Al2O3	15.17	14.63	14.79	13.40	14.41	13.63	13.65	13.94	14.41	13.57	15.1
Fe2O3	9.808	7.577	7.063	6.805	7.502	6.305	6.877	6.491	6.748	6.399	6.28
MnO	0.128	0.127	0.094	0.106	0.116	0.123	0.135	0.143	0.158	0.127	0.1
MgO	4.326	2.035	1.892	1.637	2.293	2.003	2.378	2.101	2.633	2.261	3.7
CaO	7.243	4.217	3.538	3.262	4.181	2.809	2.697	2.864	2.485	3.103	5.5
Na2O	2.138	5.401	4.885	4.889	4.589	3.346	3.284	3.635	4.269	3.320	3.2
K2O	1.518	0.711	0.735	0.783	0.914	1.739	1.574	1.753	1.213	1.635	2.4
P2O5	0.329	0.337	0.325	0.299	0.309	0.126	0.120	0.155	0.101	0.132	0.18
Au	0.001	0.002	0.014	0.003	0.003	0.001	0.001	0.001	0.001	0.001	0.003
As	46	7	13	12	17	5	4	11	2	14.45	1.7
Sb	1.9	1.7	0.9	1.4	1.33	1.5	1.1	1.3	0.6	2.335	0.3
Cu	77	96	113	82	95.5	37	38	35	37	43.1	25
Pb	2	4	6	5	4	5	6	7	4	6.6	14.8
Zn	60	49	48	44	51	62	66	64	64	64.35	65
Mo	1.1	0.7	0.6	0.6	0.7	1.9	0.7	1.7	0.5	4.155	1.1
W	1.5	2.3	3.1	3.8	2.84	0.4	0.4	0.4	0.6	0.685	1
U	0.58	0.89	0.93	0.82	0.87	2.18	1.88	1.79	1.98	2.034	8.5
Th	1.87	3.26	3.33	3.1	3.04	1.2	0.74	0.8	0.59	1.013	1.7
Zr	72.5	120.4	125.3	105.8	110.6	109.6	94.8	86.4	78	99.9	203
Nb	3.4	4.3	3.9	3.8	4.05	3.5	3.6	3.8	3.9	3.66	19
Ba	193	165	142	157	169	246	232	262	186	238.7	584
Rb	34.9	14.3	15.5	16	19.08	39	35.4	40.2	27.2	35.36	78
Sr	277.7	261.4	209.3	254.7	257.43	182.7	178.4	201.8	195.9	203.2	333
Sn	1.5	4.7	1.5	2.3	2.37	1.7	2	1.8	1.5	1.75	2.3
Be	1	0.7	0.9	0.7	0.81	1.3	1	1	0.9	1.03	2.4
Cr	50	10	8	6	24.9	40	36	34	30	38.25	126
Co	30	14.2	13.8	11.9	16.42	15.8	14.3	15.7	15.8	15.97	24
V	247	151	146	133	155.8	98	102	105	115	107.85	98
Cd	0.08	0.025	0.025	0.025	0.042	0.12	0.07	0.15	0.13	0.138	0.1
S	575	186	1050	921	653.1	695	954	5141	1389	3502	697
Y	12.9	13.5	14.5	11.3	13.07	15.7	14.6	14.5	12.5	14.76	24
La	14.5	25.7	25.9	24.1	23.42	13.5	14.2	14.3	13.9	14.9	30
Ce	32.9	56.1	56.7	52.4	51.1	30.9	32.5	33.2	31.2	33.69	60
Pr	4.59	7.55	7.53	7.1	6.90	4.26	4.52	4.7	4.23	4.61	6.7
Nd	20.4	32.3	32.8	30.4	29.58	18.7	19.9	20.2	18.3	20.07	27
Sm	4.7	6.9	6.9	6.2	6.32	4.3	4.7	4.7	4.3	4.46	5.3
Eu	1.2	1.7	1.7	1.5	1.55	1	1	1.1	0.9	1.02	1.3

	Meta-diorite (no. of samples = 10)					Meta-andesite (no. of samples = 20					
Gd	3.9	4.9	5.1	4.7	4.74	3.6	3.8	3.8	3.6	3.79	4
Tb	0.47	0.52	0.58	0.48	0.53	0.53	0.51	0.51	0.48	0.51	0.65
Dy	2.5	2.6	3.1	2.6	2.76	3	3	2.9	2.6	2.93	3.8
Ho	0.5	0.5	0.6	0.5	0.53	0.6	0.5	0.6	0.5	0.55	0.8
Er	1.3	1.3	1.6	1.3	1.39	1.8	1.7	1.7	1.5	1.69	2.1
Tm	0.2	0.2	0.2	0.2	0.2	0.3	0.3	0.2	0.2	0.26	0.3
Yb	1.2	1.3	1.5	1.2	1.34	1.8	1.7	1.6	1.6	1.72	2
Lu	0.19	0.2	0.22	0.18	0.21	0.29	0.29	0.26	0.24	0.28	0.35
∑ REEs	88.55	141.77	144.43	132.86	130.57	84.58	88.62	89.77	83.55	90.46	
Eu/Eu*	0.179	0.158	0.155	0.149	0.158	0.156	0.148	0.161	0.142	0.149	

Table 1: (continued)

	Meta-rhyodacite (no. of samples = 15)						
Sample No/oxides	345	346	347	349	350	Average (n=15)	Clarke values**
TiO2	0.294	0.241	0.275	0.204	0.279	0.263	0.68
Al2O3	14.64	13.55	15.70	13.34	13.12	13.96	15.1
Fe2O3	6.619	6.605	6.076	5.833	7.063	6.896	6.28
MnO	0.109	0.117	0.092	0.165	0.128	0.116	0.1
MgO	1.778	1.802	1.485	1.756	2.072	1.902	3.7
CaO	4.768	5.252	3.867	7.106	5.396	4.412	5.5
Na2O	3.408	2.242	1.083	0.761	2.493	2.903	3.2
K2O	1.613	1.848	3.083	2.549	1.793	1.758	2.4
P2O5	0.322	0.303	0.344	0.291	0.314	0.312	0.18
Au	0.001	0.001	0.012	0.006	0.001	0.003	0.003
As	17	18	103	65	26	33.5	1.7
Sb	1	1.2	3.6	3.8	1.7	1.73	0.3
Cu	89	51	34	67	70	80.47	25
Pb	2	2	4	4	3	3.07	14.8
Zn	69	75	83	79	79	63.53	65
Mo	0.8	0.7	0.8	1.2	1.2	0.85	1.1
W	2.4	1.6	3.1	2	1.9	2.19	1
Th	3.32	3.1	3.77	3.13	2.84	3.18	8.5
U	0.92	0.84	1.03	0.85	0.85	0.91	1.7
Zr	118	105.6	128.5	105	115.9	110.6	203
Nb	2.8	2.1	2.3	1.7	2.6	2.37	19
Ba	218	234	382	300	253	242.5	584
Rb	33.9	38.1	65.2	53.5	36.4	36.42	78
Sr	219.5	247.7	234.7	397.4	272	256.7	333
Sn	1.6	1.6	1.9	1.8	1.9	1.76	2.3
Be	1.1	1.1	1.4	1.2	1	0.99	2.4
Cr	8	2.5	2.5	2.5	7	6.3	126

	Meta-rhyodacite (no. of samples = 15)						
Co	12	11.3	13.8	11.3	12.1	12.8	24
V	141	127	151	125	127	141.9	98
Cd	0.025	0.025	0.09	0.07	0.08	0.04	0.1
S	198	203	8904	6552	1996	1834	697
Y	15.4	14.5	16.3	14.2	13.6	13.85	24
La	26.5	23.8	26.8	24.6	21.1	24.05	30
Ce	58.1	52.8	60.3	53.7	46.6	52.93	60
Pr	7.78	7.06	8.16	7.13	6.29	7.10	6.7
Nd	32.5	30.9	34.3	30.9	27	30.3	27
Sm	6.8	6.6	7.4	6.5	5.9	6.43	5.3
Eu	1.7	1.6	1.8	1.6	1.5	1.6	1.3
Gd	5.3	5.2	5.8	5.1	4.7	4.95	4
Tb	0.6	0.6	0.66	0.59	0.55	0.56	0.65
Dy	3.2	3.1	3.5	3.2	3	2.97	3.8
Ho	0.6	0.6	0.7	0.6	0.5	0.55	0.8
Er	1.6	1.5	1.7	1.5	1.5	1.48	2.1
Tm	0.2	0.2	0.2	0.2	0.2	0.2	0.3
Yb	1.6	1.4	1.6	1.4	1.3	1.39	2
Lu	0.21	0.2	0.24	0.2	0.2	0.21	0.35
∑ REEs	146.69	135.56	153.16	137.22	120.34	134.74	
Eu/Eu*	0.152	0.155	0.155	0.153	0.164	0.156	

** Upper continental crust average after Wedepohl (1995)

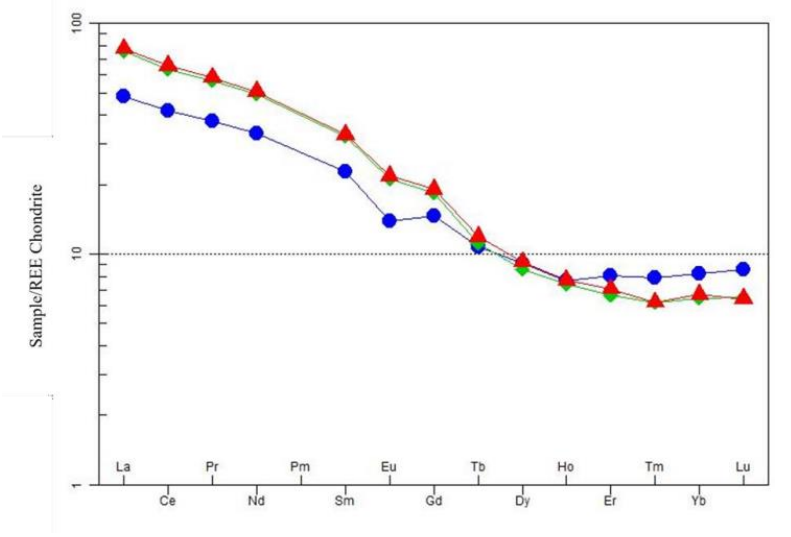

Figure 11. Chondrite normalized REE patterns for the investigated rock types in the V-Shear area. (a) meta-diorite, (b) meta-andesite, (c) meta-rhyodacite. Normalization values after [65]. Symbols as in (Figure. 8).

Table 2: Statistical distribution parameters and ranges of concentrations (in ppm) for borehole 22 (263 samples) from the V-Shear area.

Element	Range	Mini-mum	Maxi-mum	Skew Raw data	Skew Log data	Q1 25th	Q2 50th median	Q3 75th	MAD*	Thre-shold
Au	2.69	.006	2.69	6.22	1.07	0.002	0.004	0.014	0.003	0.01
As	998.00	2.00	1000	6.22	0.15	15.85	26.30	52.48	14.00	54.00
Sb	44.00	.60	44.60	8.75	1.75	1.00	1.30	1.90	0.40	2.10
Cu	264.00	14.00	278.00	2.03	0.68	37.15	46.77	75.86	14.00	75.00
Pb	16.50	.50	17.00	2.73	- 0.30	1.995	3.02	3.98	1.00	5.00
Zn	98.00	36.00	134.00	1.08	0.08	60.26	67.61	75.86	8.00	83.00
Mo	6.90	.10	7.00	3.20	0.59	0.50	0.69	1.10	0.30	1.30
Sn	9.70	.40	10.10	2.74	0.60	1.10	1.51	2.29	0.60	2.70
Be	1.65	.25	1.90	0.24	-1.03	0.60	0.80	0.90	0.20	1.20
Co	67.50	7.40	74.90	0.77	-0.24	16.22	25.12	35.48	9.60	44.30
Cr	784.50	2.50	787.00	3.24	0.04	22.91	38.90	67.61	25.00	89.00
V	340.00	33.00	373.00	1.27	-0.96	112.2	131.83	154.88	20.00	171.0
Sr	690.90	84.60	775.50	1.55	-0.12	204.2	257.04	316.23	56.30	371.4
Cd	0.72	0.03	0.74	3.55	0.35	0.06	0.08	0.10	0.02	0.12
Zr	291.90	15.30	307.20	1.50	-0.39	58.88	93.33	112.2	24.30	142.5
Y	23.50	2.90	26.40	0.91	-1.25	12.88	14.13	15.49	1.40	17.00
S	32767	25.00	32792	5.63	0.07	114.8	354.8	1096.5	329	1012

* Median Absolute Deviation

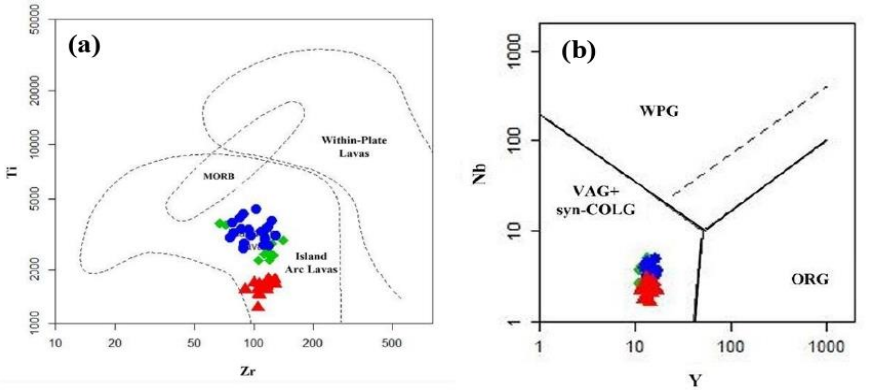

Figure 12. Tectonic discrimination diagrams for the investigated rock types. (a) Zr vs. Ti diagram after [45], (b) Y vs. Nb diagram after [46]. WPG = within plate granite, ORG = ocean ridge granite, VAG = volcanic arc granite and COLG = collision granite. Symbols as in (Figure. 9).

Table 3: Statistical distribution parameters and ranges of concentrations (in ppm) for borehole 25 (231 samples) from the V-Shear area.

Element	Range	Mini-mum	Maxi-mum	Skew Raw data	Skew Log data	Q1 25th	Q2 50th (Median)	Q3 75th	MAD*	Thre-shold
Au	0.06	0.006	.056	6.22	1.53	0.0005	0.001	0.002	0.001	0.002
As	124.90	0.10	125.00	3.50	0.09	0.69	2.19	12.88	1.80	5.80
Sb	17.30	0.20	17.50	1.75	0.63	0.50	0.90	2.94	0.50	1.90
Cu	136.00	13.00	149.00	0.07	-0.81	60.26	81.28	109.65	24.00	130.0
Zn	127.00	27.00	154.00	0.60	-1.08	70.79	79.43	87.10	8.00	95.0
Sn	4.60	0.40	5.00	2.54	0.82	0.50	0.60	1.29	0.10	0.80
Be	2.15	0.25	2.40	1.01	0.05	0.25	0.60	1.0	0.35	1.30
Li	47.00	2.80	49.80	1.92	-0.60	12.02	14.79	17.38	2.50	19.90
Ni	423.50	0.50	424.00	1.49	0.17	15.14	36.31	56.23	21.00	78.00
Cr	470.00	16.00	486.00	0.65	-0.26	34.67	120.23	234.42	89.00	299.0
V	393.00	40.00	433.0	-0.36	-1.03	173.78	288.4	346.74	79.00	448.0
Ba	404.00	6.00	410.00	0.78	-0.11	25.00	57.54	181.97	40.00	137.0
Rb	54.65	0.05	54.70	0.88	-0.12	0.40	2.69	23.44	2.60	7.90
Sr	700.70	109.50	810.20	0.50	-0.28	218.78	331.13	446.68	112.9	557.7
Cd	0.58	0.03	0.60	2.11	-0.04	0.09	0.12	0.16	0.03	0.18
Zr	308.40	9.40	317.80	1.59	0.59	16.60	19.95	95.50	6.20	32.50
Y	26.80	5.10	31.90	1.23	0.21	7.76	9.12	13.80	2.10	13.30
S	17166	25.00	17191	2.18	0.17	85.11	239.88	3311.3	212.0	661.0

* Median Absolute Deviation

Comparing median values of the chosen elements in the investigated boreholes (Tukey Box plot of (**Figure 13**) revealed the following: Borehole 22 has more median concentrations of Au, As, Sn, Be, Zr, and Y and lower median concentration of Cu, Zn, Cr, V, Sr, and Cd and comparable median concentrations of Sb, and S compared with borehole 25. The threshold values of the selected trace elements were determined (Table 4) and the number of anomalous values were counted for Au, being 25 and 17 samples in BH22 and BH25, respectively, indicating the relative higher ore potentiality of borehole 22. Base metal (e.g., Cu, Zn) anomalous samples are also more abundant in BH22 (being 60 and 34 samples for Cu and Zn, respectively) compared with those recorded in BH25 (being 14 and 12 samples for Cu and Zn, respectively).

6.2. Enrichment and depletion of trace elements

The calculated threshold value of the selected trace elements in each borehole was divided by that of the least altered un-mineralized wallrock (average of 80 samples) to determine their enrichment factors (EF) as described by [47] according to the equation:

$$EF = [\text{median} + 2\text{MAD}]_{\text{rock sample borehole}} / [\text{median} + 2\text{MAD}]_{\text{least altered wallrock}}$$

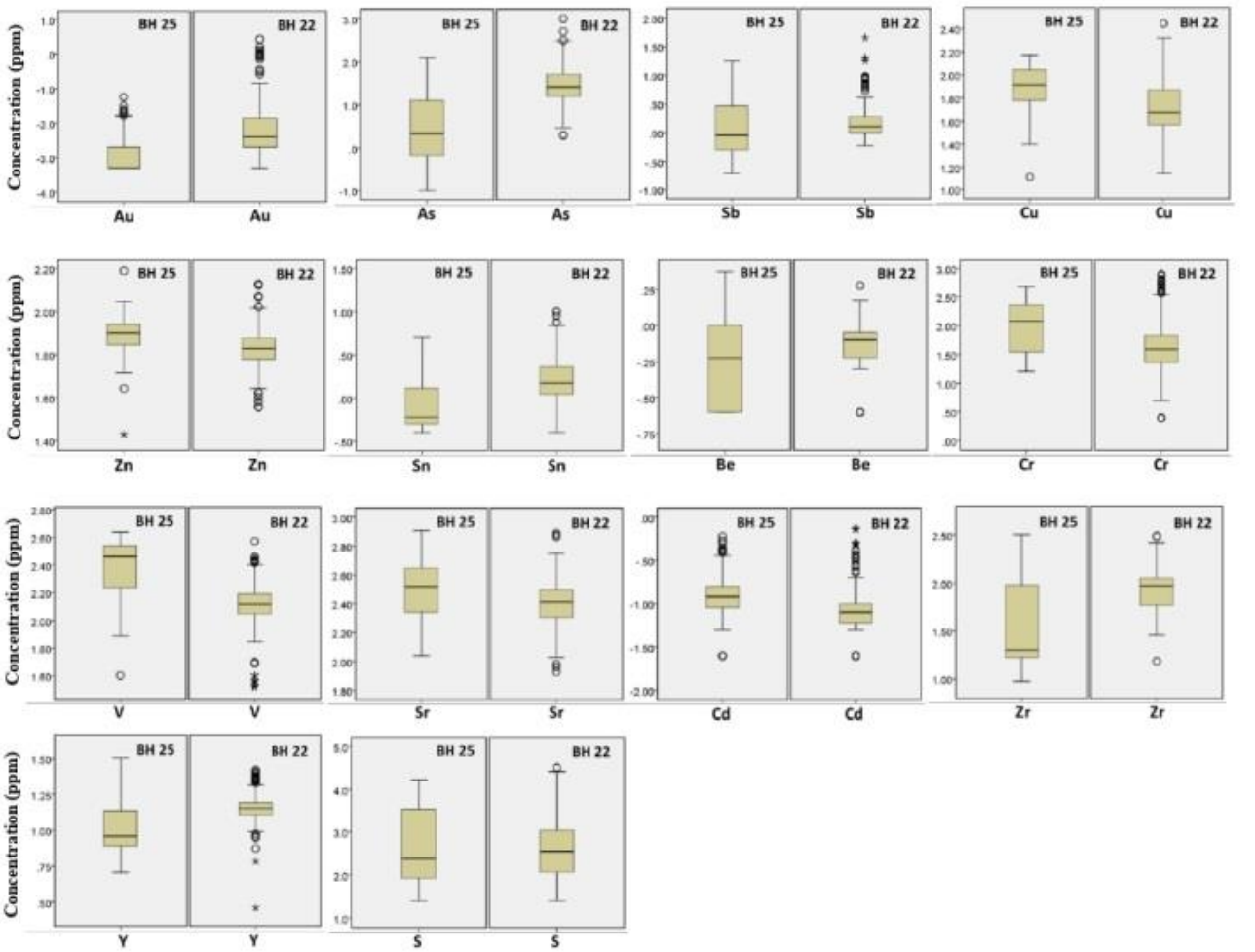

Figure 13. Tukey boxplots of Au, As, Sb, Cu, Zn, Sn, Be, Cr, V, Sr, Cd, Zr, Y, and S (ppm; transformed to base 10 logarithms) in the investigated boreholes in the V-Shear area.

The results are presented in (Table 4) considering the following range's scale: EF > 5 = strongly enriched; EF 5-2 = moderately enriched; EF 2-1 = weakly enriched; EF 1-0.5 = weakly depleted; EF < 0.5 strongly depleted. As shown in (Table 4), borehole 22 is weakly enriched in Au, Sb, Cu, Pb, Zn, Mo, Sn, Be, Co, Cr, V, and Zr. On the other hand, BH22 is weakly depleted in As, S, Sr, Cd, and Y. In contrast, borehole 25 is strongly enriched in Cr, moderately enriched in V and Cu, and weakly enriched in Zn, Ni, Sr, Cd, Li, and Be. On the other hand, BH25 is strongly depleted in Au, As, Ba, Rb, Sn, Zr, and S, and weakly depleted in Y.

6.3. Factor analysis

To study the multi-element associations that might exist in the study boreholes of the V-Shear area, orthogonal R-mode factor analysis according to the principal factoring method after [48] was applied concerning those elements that have the best distribution tendencies in each borehole of the study area using SPSS software program. To overcome the closure problem in multivariate statistical analysis of compositional datasets [40], centered log-ratio (CLR) transformation [38] for the elemental data was carried out prior to factor analysis. [41] criterion to extract only factor loadings with eigenvalues greater than 1 was applied. The extracted factor loadings were subjected to orthogonal rotation by the Varimax method to maximize the variability among all input data. The broken-stick method [42] was applied to determine which factor loading is significant. The factor matrix of the CLR data of the investigated boreholes is summarized in (Table 5).

Five factors were extracted, explaining 73.079 % of the total variance. Factor 1 (ca. 19.54% of multivariate data variability) represents an association of Sn, Be, Zr, Y, and Ba and is considered a granitic wallrock controlling factor with signs of alteration. Factor 2 (ca. 16.75% of multivariate data variability) represents an association of Sb, Pb, Mo, Cd, and S and reflects base metal and sulfide associations. Factor 3 (ca. 14.52% of multivariate data variability) represents an association of Ni, Co, Cr, and Li and reflects the surrounding mafic country rocks. The existence of Li among this association may reflect pegmatite or greisen rocks

Table 4: Threshold values and Enrichment Factors of the selected trace elements in the investigated boreholes of the V-Shear area**.**

Element	Median*	MAD*	Threshold*	EF (22)**	EF (25)**
Au	0.002	.0015	0.01	1.00	0.20
As	23.50	15.50	54.50	0.99	0.11
Sb	1.25	0.35	1.95	1.08	0.97
Cu	39.00	7.50	54.00	1.39	2.41
Pb	3.00	1.00	5.00	1.00	-----
Zn	66.00	5.00	76.00	1.09	1.25
Mo	0.80	0.20	1.20	1.08	-----
Sn	1.80	0.40	2.60	1.04	0.31
Be	0.90	0.10	1.10	1.09	1.18
Li	10.15	2.15	14.45	-----	1.38
Ni	28.50	5.50	39.50	-----	1.97
Co	20.25	4.35	28.95	1.53	-----
Cr	35.50	7.50	50.50	1.76	5.92
V	109.00	9.00	127.00	1.35	3.53
Ba	202.50	40.50	283.50	-----	0.48
Rb	29.75	8.20	46.15	-----	0.17
Sr	294.70	67.95	430.60	0.86	1.30
Cd	0.095	0.025	0.15	0.80	1.20
Zr	102.50	12.55	127.60	1.12	0.25
Y	14.80	1.30	17.40	0.98	0.76
S	954.0	733.0	2420.0	0.42	0.27

* Data for least altered un-mineralized samples

** Data for the study boreholes

MAD: Median absolute deviation; EF: Enrichment factor

Factor 4 (ca. 13.39% of multivariate data variability) represents an association of Cu, Zn, V, and Sr and reflects base-metal-related mafic rocks and alteration associations. Factor 5 (ca. 8.88% of multivariate data variability) represents an association of Au and As and reflects gold mineralization associated with arsenian. This factor has the lowest value of data variability reflecting the poor gold potentiality in the study boreholes.

7. Discussion

The majority of gold mineralization in the Eastern Desert is associated with quartz veins that were formed during Late Neoproterozoic ore-forming events [6, 49]. Most of these quartz veins are hosted in metamorphic rocks that have undergone greenschist/amphibolite facies metamorphism and are associated with un-metamorphosed granitic intrusions. The distribution of the auriferous quartz veins is controlled by major faults (7, 10, 50, 11) which mainly related to brittle-ductile shear zones. These shear zones that strike NW- and/ or NNW almost control the channel ways of hydrothermal fluids and finally host the mineralized veins.

7.1. Classification of the V-Shear gold mineralization

Gold mineralization in the V-Shear area has geological setting, structural, mineralogical, and alteration style that make features suggestive of the broad class orogenic gold type. It occurs within the greenschist/amphibolite facies arc metamorphic rocks in association with late tectonic unmetamorphosed granitic intrusions. This matches with the vast majority of orogenic auriferous quartz veins in the Eastern Desert that crosscut 800–640 Ma arc metamorphic rocks and intruded by late tectonic ca. 650–600 Ma unmetamorphosed granitic masses [8, 9, 10, 26, 6, 51]. [49] suggest that the orogenic gold deposits in the Eastern Desert have been formed by ~600Ma.

One of the main factors controlling the mineralization of the Orogenic gold deposits is the structural elements. Shearing and fracturing are intense in the V-Shear area, where the mineralized quartz veins are controlled. The quartz veins are almost trending NE and dipping due to W following the regional structure orientation. This pattern confirms that NE–SW-trending structures played a major role in localizing gold mineralization in the Eastern Desert. The shear zones and their associated auriferous quartz veins cut all the rock types and are consequently interpreted to be younger in the timing of formation.

The formation of orogenic gold deposits worldwide reflects the passage of large volumes of hydrothermal fluids through permeable channel ways in a brittle structure environment [52, 5]. Such fluids tend to have a common composition with low salinities and high CO_2 contents, and deposition typically occurs at a temperature of approximately 350 °C and depths of 4 - 12 km [4]. In agreement, the fluids responsible for the gold precipitation at the V-Shear area are thought to be a mixture of aqueous and carbonic fluids characterized by low salinities and alkaline to neutral pH. The abundance of H_2O-bearing minerals (e.g., sericite and chlorite) and carbonates may support this assumption (**Figure 6g-i**).

Sulfide mineralogy of the orogenic gold deposits in the Eastern Desert is dominated by pyrite, arsenopyrite, and pyrrhotite, in addition to subordinate chalcopyrite, sphalerite, galena, and tetrahedrite [6, 49]. In the V-Shear area, the hydrothermal sulfide minerals are frequently observed in the quartz veins and the alteration zones and are dominated by the formation of pyrite and arsenopyrite and less common chalcopyrite, pyrrhotite, and sphalerite.

Table 5: Varimax rotated R-mode factor matrix with Kaiser Normalization for the investigated boreholes CLR* data in the V-Shear area.

Element	Factor				
	1	2	3	4	5
Au	.185	-.095	.045	.075	.805
As	-.033	.317	-.183	-.270	.754
Sb	.114	.718	.309	-.116	.228
Cu	-.256	.056	-.267	.719	-.014
Pb	.442	.733	-.146	.024	.018
Zn	.123	.002	.237	.826	-.009
Mo	.232	.693	.053	-.022	-.132
Sn	.642	.073	-.219	-.014	.464
Be	.715	.438	-.175	-.070	-.088
Li	-.045	-.170	.688	-.114	-.199
Ni	-.077	.476	.728	-.112	.102
Co	-.551	-.092	.710	.203	-.032
Cr	-.135	.508	.758	-.009	-.021
V	-.586	-.052	.017	.718	-.205
Ba	.603	.202	-.437	-.377	.128
Rb	.422	.028	-.410	-.520	.413
Sr	-.279	-.140	-.157	.595	.007
Cd	.104	.626	.366	.209	-.031
Zr	.871	.246	-.145	-.172	.135
Y	.859	.061	.105	-.223	.043
S	.027	.796	-.237	-.207	.231
Eigen values	4.103	3.517	3.049	2.812	1.865
% of variance	19.538	16.750	14.519	13.391	8.881
Cum% of variance	19.538	36.288	50.807	64.198	73.079

* Centered Log Ratios

7.2. Petrogenesis of the least altered rocks

The meta-diorites, meta-andesites, and meta-rhyodacites of the V-Shear area are characterized by calc-alkaline nature (**Figure 9a**) and enrichment in LREE over HREE (**Figure 11**). These features are consistent with subduction zone-related magmas [53, 54, 55]. The low contents of HFSEs (e.g., Nb, Ta) in the studied rocks support this interpretation. The tectonic setting of the studied rocks as deduced from the discrimination diagrams (**Figure 12**) confirms their formation in an arc setting. Oceanic arc rather than continental arc setting can be inferred based on our available trace element data, where all the investigated rock types have low contents of LILEs (e.g., Rb, Ba, Sr) besides HFSEs [56]. In spite of pertaining to the same tectonic setting, and sharing some geochemical characters, the absence of co-linear trends between Rb and K/Rb on one hand and Ba-Sr, Rb-Sr on the other (as noticed in (**Figure 10**) suggests the derivation of the studied rocks from independent magma batches rather than from one continuous series.

On the other hand, the depleted contents of Cr and Ni in meta-diorites may indicate that some kind of differentiation (e.g., fractional crystallization of pyroxene) has taken place. On the other hand, the depletion of Sr and Ba in the investigated rock

types reflects either fractional crystallization of plagioclase feldspar [57, 58] or derivation from upper mantle sources already poor in such incompatible elements [59]. The impoverishment of other incompatible elements (e.g., Rb, Cs) and HFSEs (**Figure 8**), along with the plotting of the studied rock samples in the less-differentiation field (**Figure 10c**) support the latter interpretation. In addition, the very weak/absence of negative Eu anomaly (**Figure 11**) may uphold this interpretation. However, the weak negative Eu anomaly exhibited by the meta-andesite samples implies that the fractional crystallization of plagioclase during the formation of this rock variety cannot be ruled out.

7.3. Genetic aspects

The available data obtained from the present study refer to that the gold mineralization in the V-Shear area is of post-date regional metamorphism. The post-peak metamorphic origin is supported by the following features: (i) Many corroded inclusions of undigested wall rock materials are preserved as relics in younger sulfide minerals (e.g., pyrite and arsenopyrite) (**Figures 7c & d**). Clear that some of these relics constitute parts of the metamorphic rock units in the study area, (ii) many sulfides are characterized by their replacement and fracture-filling textures reflecting sulfidation of preexisting the host metamorphic rocks as well as the granitic intrusions, (iii) sulfide minerals and quartz are distributed over different parageneses indicating various stages of mineralization, and (iv) the mineralized quartz veins are almost localized along the contacts between the metavolcanic and metagabbro-diorite rocks and/or cross-cut all the units.

As the hydrothermal process is the main event at the study V-Shear prospect area, the gold mineralization can be divided into three stages, each distinct with mineral assemblages: pre-, main, and post-hydrothermal (**Figure 14**). Minerals of the pre-hydrothermal assemblage are disseminated in the fresh host rocks and may occur as relics in the altered rocks and quartz veins. The pre-hydrothermal assemblage includes ore minerals of magmatic and metamorphic origin. Chromite, ilmenite, and titanomagnetite are the main oxide minerals and are chiefly disseminated in the metavolcanic and metagabbro-diorite rock units. Part of the pyrrhotite and chalcopyrite represent the primary sulfide minerals and are almost confined to the least altered meta-andesite and metadioritic rocks. The entire basement rocks at the V-Shear area have been undergoing low-grade greenschist facies metamorphism. During the metamorphic event, rutile ± anatase has been formed almost from Ti-bearing minerals (e.g., ilmenite and titanomagnetite), whereas chromite may transform to ferritchromit.

The bulk of alteration and sulfide minerals as well as free gold are younger than magmatic and metamorphic opaque minerals and consequently are of post-peak-metamorphic hydrothermal origin. The petrographic study indicates that the investigated fresh rocks have been affected strongly by hydrothermal alteration. Sericitization, carbonatization, chloritization, silicification, and sulfidation are the most common alteration processes. Based on the textural analysis, the early stage has participated in the development of the hydrous minerals (i.e., sericite, chlorite) to a regional extent. Consequently, initial high K+ and H+ activities are suggested for the invading fluids. The progressive formation of sericite and chlorite consumes H^+, raises pH, and makes the fluid more alkaline with a relatively high CO_2/H_2O ratio and S. Under these conditions, solubility of Au has been reduced allowing Au and sulfides to precipitate.

Hydrothermal sulfides formed in two distinct features; replacements and fracture-fillings. Replacement sulfide minerals (i.e., pyrite and arsenopyrite) were formed by the sulfidation of pre-existing rocks, particularly their disseminated pyrrhotite and chalcopyrite as a result of the increase of fS_2 from the mineralizing solutions. Both pyrite and arsenopyrite hold a lot of wall rock materials, and rutile inclusions (**Figure 7c & d**) in addition to pyrrhotite and chalcopyrite (**Figure 7e**). Fracture-filling sulfides include mainly chalcopyrite, sphalerite, and free gold (**Figure 7c**).

It is realistic to postulate that the quartz veins in the study mine area were formed as a result of a strong and prolonged stage of fracture growth and opening associated with continuous crystallization of quartz. A later surge of fluid has resulted in the silicification of the preexisting wall rock and the formation of the quartz vein. All the studied minerals are partially or completely silicified during the last stage of alteration. Native gold and sulfide minerals are not paragenetically associated with quartz, but only represent the last stable minerals in SiO_2-rich solution and consequently they are enriched in zones where SiO_2-rich solution was able to infiltrate into the wall rocks.

The post-hydrothermal assemblage includes the oxide and hydroxide minerals that formed under supergene conditions e.g., goethite ± lepidochrocite, leucoxene

7.4. Geochemical exploration features

The statistical analysis of two borehole data sets including 17 trace elements has been conducted using both univariate and multivariate statistical approaches. To avoid the effect of outlier values on the calculated backgrounds we used median rather than geometric mean [37]. For comparing the individual background values in the selected boreholes (BH22 and BH25), Whisker box plots [60] were constructed and examined. Higher background concentrations of Au, As, Sn, Be, Zr, and Y were detected in BH22, located about 1 Km to the SE of BH25. Threshold values calculated from median and median absolute deviation (MAD) exhibited the existence of anomalous values in both boreholes (being 25 and 17 samples in BH22 and BH25, respectively). However, the calculated enrichment factor (EF) after [47] for Au and the associated trace elements revealed that BH22 is weakly enriched in Au, Sb, Cu, Pb, Zn, Mo, Sn, Be, Co, Cr, V, Zr and weakly depleted in As, S, Sr, Cd, Y. By contrast, BH25 is strongly depleted in Au, As, Ba, Rb, Sn, Zr, and S and enriched in Cr, V, Cu, and weakly enriched in Zn, Ni, Sr, Cd, Li, and Be.

R-mode factor analysis was applied to the borehole data sets. Centered log ratios (CLR) rather than logarithmic values were used to address the problem of closed compositional data [38]. The significant loadings are more than +0.5 and less than – 0.5 (or > 0.5 as an absolute value). Five factors were extracted and found to represent five main associations (arranged in descending order of data variability): (i) Felsic wallrock association (F1) represented by Sn, Be, Zr, Y, (Co, V) and Ba; (ii) Sulfides association (F2) represented by Sb, Pb, Mo, Cd, (Cr) and S; (iii) Mafic wallrock association (F3)

represented by Ni, Co, Cr, and Li; (iv) Base metal association (F4) represented by Cu, Zn, V, Rb and Sr; and (v) Gold association (F5) represented by Au and As. Among all factors, the Au-controlled one has the lowest value of data variability (ca. 8.88%) and this may support our finding about the poor gold potentiality in the study boreholes. The existence of arsenic among the Au-factor loads suggests using arsenic as a good indicator for gold in the study area.

Minerals	Pre-hydrothermal assemblage (Initial rock or least altered rock)		Post-metamorphic (hydrothermal) assemblages			Weathering assemblage
			Early	Late		
	Magmatic assemblage	Metamorphic assemblage	Replacement assemblage	Fracture-filling assemblage	Quartz vein	
Chromite	X					
Rutile		XX				
Pyrrhotite	X					
Arsenopyrite			XXX			
Pyrite			XXX			
Chalcopyrite	X		X	X		
Sphalerite			X	X		
Native gold				X		
Sericite			XXX			
Carbonate			XXX	X	X	
Chlorite			XXX	X		
Epidote			XX			
Quartz			X	X	XXX	
Leucoxene						XX
Lepidocrocite						XX
Goethite						XX

Figure 14. Paragenetic sequence of alteration and ore minerals. The intensity of lines refers to the mineral abundance.

Conclusions

- Gold mineralization in the V-Shear prospect area is mainly localized within the meta-andesites, metagabbro-diorite, and along their contacts. These main rock types have a calc-alkaline affinity of island arc tectonic setting. This may indicate that gold mineralization in the study area is related to the subduction process and its structural controls. The entire rock units have suffered greenschist/amphibolite facies metamorphism
- Tectonism has resulted in well-developed shear planes and foliation in the wall rock. The gold mineralization is linked with the NE-trending shear zones and dipping due to W following the regional structure orientation NE-trending Najd Fault System.
- Field and petrographic investigations revealed that the gold mineralization resulted in the circulation of aqueous and carbonic fluids related to post-peak metamorphic hydrothermal activity.
- Three stages of mineralization have been identified namely; pre-hydrothermal, hydrothermal, and post-hydrothermal. The hydrothermal sulfide phases include pyrite, and arsenopyrite, and subordinate pyrrhotite, chalcopyrite, and sphalerite. Part of these sulfides is formed as a result of the sulfidation of pre-existing rocks.
- Univariate statistical analysis of the borehole data sets from the V-Shear area revealed low ore potentiality as reflected by the weak to very weak enrichment factor of gold in the study boreholes. However, the southeastern borehole (BH22) has a relatively higher EF than the northeastern one (BH25) (being 1 and 0.2, respectively).
- Element associations derived from R-mode factor analysis are represented by five significant ones, namely felsic wallrock association, sulfides association, mafic wallrock association, base metal association, and gold association.
- The existence of arsenic along with gold in the mineralization-controlled factor suggests using arsenic as a good indicator for gold in the study area. This may also indicate the existence of gold in arsenopyrite.

Acknowledgment

The authors would like to express their truthful gratitude and appreciation to the “Sukari Gold Mines” company with special thanks to Mr. Sami El-Raghy, Centamin PLC, for allowing us

to conduct this study and for the great facilities he made to achieve this work. Thanks also to Mr. Mohamed El-Behairy, senior exploration geologist in the Sukari gold mine for his assistance in providing the drill core and gold data used in this study. We are also grateful to Prof. Dr. Hanafy M. Holail for his continuous support and help.

References

[1] Hussein, A.A.; El-Sharkawi, M.A. Mineral deposits in: Said, R., (Ed.), The Geology of Egypt. A.A. Balkema, Rotterdam/ Brookfield. 1990, 511-566.
[2] Botros, N.S. New prospects for gold mineralization in Egypt. Ann. Geol. Surv., Egypt. 1993, 19, 47-56.
[3] Groves, D.I.; Goldfarb, R.J.; Gebre-Mariam, M.; Hagemann, S.G.; Robert, F. Orogenic gold deposits: a proposed classification in the context of their crustal distribution and relationship to other gold deposit types. Ore Geol. Rev. 1998, 13, 7–27.
[4] Goldfarb, R.J.; Groves, D.I.; Gardoll, S. Orogenic gold and geologic time: a global synthesis. Ore Geol. Rev. 2001, 18(1-2), 1-75.
[5] Goldfarb, R.J.; Baker, T.; Dube, B.; Groves, D.I.; Hart, C.J.; Gosselin, P. Distribution character and genesis of gold deposits in metamorphic terranes. In: Hedenquist, J.W., Thompson, J.F.H., Goldfarb, R.J., Richards, J.P. (Eds.), Economic Geology 100th Anniversary volume. 2005, 407-450.
[6] Khalil, I.K.; Moghazi, A.M.; El Makky, A.M. Nature and geodynamic setting of late Neoproterozoic vein-type gold mineralization in the Eastern Desert of Egypt: mineralogical and geochemical constraints. In: Bouabdellah, M., Slack, J.F. (Eds.), Mineral deposits of North Africa, Berlin-Heidelberg, Springer-Verlag, 2016, 353-370.
[7] Loizenbauer J.; Neumayr P. Structural controls on the formation of the Fawakhir gold mine, EL Sid-Eastern Desert, Egypt: tectonic and fluid inclusion evidence. In: Proceedings of the Geological Survey of Egypt centennial conference, Geol. Surv. Egypt, 1996, 477-488.
[8] Kusky, T.M.; Ramadan, T.M. Structural controls on Neoproterozoic mineralization in the South Eastern Desert, Egypt: an integrated field, Landsat TM, and SIR-C/X SAR approach. J. Afr. Earth Sci. 2002, 35(1), 107-121.
[9] Botros, N.S. A new classification of the gold deposits of Egypt. Ore Geol. Rev. 2004, 25(1-2), 1-37.
[10] Helmy, H.M.; Kaindl, R.; Fritz, H.; Loizenbauer, J. The Sukari Gold Mine, Eastern Desert—Egypt: structural setting, mineralogy and fluid inclusion study. Mineral. Deposita. 2004, 39, 495-511.
[11] Zoheir, B. Transpressional zones in ophiolitic mélange terranes: potential exploration targets for gold in the South Eastern Desert, Egypt. J. Geochem. Exploration. 2011, 111(1-2), 23-38.
[12] Zoheir, B.A.; Emam, A.; Pitcairn, I.K.; Boskabadi, A.; Lahaye, Y.; Cooper, M.J. Trace elements and isotopic data of the Um Garayat gold deposit, Wadi Allaqi district, Egypt. Mineral. Deposita. 2018, 54 (1), 101-116.
[13] Harraz, H.Z. A genetic model for a mesothermal Au deposit: evidence from fluid inclusions and stable isotopic studies at El Sid Gold Mine, Eastern Desert, Egypt. J. Afr. Earth Sci. 2000, 30(2), 267-282.
[14] Botros, N.S. Metallogeny of gold in relation to the evolution of the Nubian Shield in Egypt. Ore Geol. Rev. 2002, 19, 137–164.
[15] Khalil, I.K.; Helba, H.A.; Mucke, A. Genesis of the gold mineralization at the Dungash gold mine area, Eastern Desert, Egypt: a mineralogical-microchemical study. J. Afr. Earth Sci. 2003, 37 (1-2), 111–122.
[16] Zoheir, B.A.; Akawy, A. Genesis of the Abu Marawat gold deposit, central Eastern Desert of Egypt. J. Afr. Earth Sci. 2010, 57 (4), 306–320.
[17] El-Makky, A.M.; Khalil, K.I.; Ibrahim, I.M. Hydrothermal wall rock alteration at Kurdeman gold mine area, Eastern Desert, Egypt. Neues Jb. Mineral. Abh. 2012, 189 (1), 75–95.
[18] Helmy, H.M.; Zoheir, B.A. Metal and fluid sources in a potential world-class gold deposit: El-Sid mine, Egypt. Int. J. Earth Sci. 2015, 104, 645–661.
[19] Abd El-Wahed, M.A.; Harraz, H.; El-Behairy, M.H. Transpressional imbricate thrust zones controlling gold mineralization in the Central Eastern Desert of Egypt. Ore Geol. Rev. 2016, 78, 424-446.
[20] El Makky A. M.; and Feteha B. F. Geochemical data interpretation and vertical zoning of Au-associated elements at the Sukari mine area, central Eastern Desert, Egypt. Egyptian Mineralogist, 2014
[21] Harraz, H.Z. Primary geochemical haloes, El Sid Gold Mine, Eastern Desert, Egypt. J. Afr. Earth Sci. 1995, 20, 61–71.
[22] Harraz, H.Z.; Hamdy, M.M. Zonation of primary haloes of Atud auriferous quartz vein deposit, Central Eastern Desert of Egypt: A potential exploration model targeting for hidden mesothermal gold deposits. J. Afr. Earth Sci. 2015, 101, 1–18.
[23] Helba, H.A.; Khalil, K.I.; Mamdouh, M.M.; Abd El-Khalek, I.A. Zonation in primary geochemical haloes for orogenic vein-type gold mineralization in the Quartz Ridge prospect, Sukari gold mine area, Eastern Desert of Egypt. J Geochem. Exploration. 2020, 209, 106378.
[24] Vail, J.R. Tectonics and evolution of the Proterozoic basement of northeastern Africa. In: El Gaby, S., Greiling, R.O. (Eds.). The Pan-African belt of Northeast Africa and adjacent areas: tectonic evolution and economic aspects of a late Proterozoic Oregon. 1988, 195-226.
[25] Klemm, D.; Klemm, R.; Murr, A. Gold of the Pharaohs–6000 years of gold mining in Egypt and Nubia. J. Afr. Earth Sci. 2001, 33(3-4), 643-659.
[26] Gabr, S.; Ghulam, A.; Kusky, T. Detecting areas of high-potential gold mineralization using ASTER data. Ore Geol. Rev. 2010, 38(1-2), 59-69.
[27] Johnson, P.R.; Andresen, A.; Collins, A.S.; Fowler, A.R.; Fritz, H.; Ghebreab, W.; Kusky, T.; Stern, R.J. Late Cryogenian–Ediacaran history of the Arabian–Nubian Shield: a review of depositional, plutonic, structural, and tectonic events in the closing stages of the northern East African Orogen. J. Afr. Earth Sci. 2011, 61(3), 167-232.

[28] Abdel Khalek, M.L. Tectonic evolution of the basement rocks in the Southern and Central Eastern Desert of Egypt. Bull Inst Appl Geol., King Abdel Aziz Uni., Jeddah. 1979, 3(1), 53-62.
[29] Stern, R.J.; Hedge, C.E. Geochronologic and isotopic constraints on late Precambrian crustal evolution in the Eastern Desert of Egypt. Am. J. Sci. 1985, 285(2), 97-127.
[30] El-Gaby, S.; List, F.K.; Tehrani, R. Geology, evolution and metallogenesis of the Pan-African belt in Egypt. In: El Gaby, S., Greiling, R.O. (Eds.). The Pan-African belt of Northeast Africa and adjacent areas: tectonic evolution and economic aspects of a late Proterozoic Oregon. 1988, 17-68.
[31] Shackleton, R.M.; Ries, A.C.; Graham, R.H.; Fitches, W.R. Late Precambrian Ophiolitic melange in the Eastern Desert of Egypt. Nature. 1980, 285, 472-474.
[32] Ries, A.C.; Shackleton, R.M.; Graham, R.H.; Fitches, W.R. Pan-African structures, ophiolites and mélange in the Eastern Desert of Egypt: a traverse at 26 N. J. Geol. Society. 1983, 140(1), 75-95.
[33] El-Gaby, S.; List, F.K.; Tehrani, R. The basement complex of the Eastern Desert and Sinai: 1990, 175–184. In: Said, R. (Ed.). The Geology of Egypt. A.A. Balkema, Rotterdam.
[34] El Bahariya, G. Classification of the Neoproterozoic ophiolites of the Central Eastern Desert, Egypt based on field geological characteristics and mode of occurrence. Arabian Journal of Geosciences. 2018, 11, 1-23.
[35] Stern, R.J. Neoproterozoic formation and evolution of Eastern Desert continental crust–The importance of the infrastructure-superstructure transition. J. Afr. Earth Sci. 2018, 146, 15-27.
[36] Stern, R.J.; Ali, K. Crustal evolution of the Egyptian Precambrian rocks. In: Hamimi Z., El-Barkooky A., Fairs, J., Fritz, H., Abd El-Rahman, Y., (Eds.). The Geology of Egypt. 2020, 131-151.
[37] Reimann, C.; Filzmoser, P.; Garrett, R.G. Background and threshold: critical comparison of methods of determination. Science of the Total Environment. 2005, 346(1-3), 1-16.
[38] Aitchison, J. The statistical analysis of compositional data. Chapman and Hall, London. 1986, 416 p.
[39] Carranza, E.J.M. Analysis and mapping of geochemical anomalies using log-ratio-transformed stream sediment data with censored values. J. Geochem. Exploration. 2011, 110(2), 167-185.
[40] Reimann, C.; Filzmoser, P.; Garrett, R.; Dutter, R. Statistical data Analysis Explained: Applied Environmental Statistics with R. John Wiley & Sons, Ltd. 2008, 362p.
[41] Kaiser, H.F. The application of electronic computers to factor analysis. Educational and psychological measurement. 1960, 20(1), 141-151.
[42] Peres-Neto, P.R.; Jackson, D.A.; Somers, K.M. Giving meaningful interpretation to ordination axes: assessing loading significance in principal component analysis. Ecology. 2003, 84(9), 2347-2363.
[43] Ishikawa, Y.; Sawaguchi, T.; Iwaya, S.; Horiuchi, M. Delineation of prospecting targets for Kuroko deposits based on modes of volcanism of underlying dacite and alteration haloes. Mining Geol. 1976, 26(136), 105-117.
[44] Mathieu, L. Quantifying hydrothermal alteration: a review of methods. Geosci. 2018, 8(245), 1–27.
[45] Pearce, J.A. Trace element characteristics of lavas from destructive plate boundaries. In: Thorpe, R.S. (Ed.). Orogenic andesites and related rocks, John Wiley and Sons Ltd. 1982, 528-548.
[46] Pearce, J.A.; Harris, N.B.; Tindle, A.G. Trace element discrimination diagrams for the tectonic interpretation of granitic rocks. J. Petrol. 1984, 25(4), 956-983.
[47] Wang, G.; Pang, Z.; Boisvert, J.B.; Hao, Y.; Cao, Y.; Qu, J. Quantitative assessment of mineral resources by combining geostatistics and fractal methods in the Tongshan porphyry Cu deposit (China). J. Geochem. Exploration. 2013, 134, 85-98.
[48] Harman, H.H. Modern factor analysis. University of Chicago Press, Chicago, III. 1976, 487.
[49] Zoheir, B.A.; Johnson, P.R.; Goldfarb, R.J.; Klemm, D.D. Orogenic gold in the Egyptian Eastern Desert: Widespread gold mineralization in the late stages of Neoproterozoic orogeny. Gondwana Res. 2019, 75, 184-217.
[50] Zoheir, B.A. Structural controls, temperature–pressure conditions and fluid evolution of orogenic gold mineralization at the Betam mine, south Eastern Desert, Egypt. Mineral. Deposita. 2008a, 43, 79-95.
[51] Zoheir, B.; Emam, A.; El-Amawy, M.; Abu-Alam, T. Auriferous shear zones in the central Allaqi-Heiani belt: Orogenic gold in post-accretionary structures, SE Egypt. J. Afr. Earth Sci. 2017, 146, 118-131.
[52] Sibson, R.H.; Robert, F.; Poulsen, K.H. High-angle reverse faults, fluid-pressure cycling, and mesothermal gold-quartz deposits. Geology. 1988, 16(6), 551-555
[53] Kelemen, P.B.; Hanghøj, K.; Greene, A.R. One view of the geochemistry of subduction-related magmatic arcs, with an emphasis on primitive andesite and lower crust. In: Holland, H.D., Turekian, K.K. (Eds.), Treatise on Geochemistry. Elsevier, Amsterdam. 2014, pp. 749-806. 2nd edition DOI 10.1016/B978-0-08-095975-7.00323-5.
[54] Pearce, J.A.; Stern, R.J. Origin of back-arc basin magmas: Trace element and isotope perspectives. In: Christie, D.M., Fisher, C.R., Lee, S.M. and Givens, S. (Eds.), Back-Arc Spreading Systems; Geological, Biological, Chemical, and Physical Interactions. Geophysical Monograph Series 166, American Geophysical Union, Washington, 2006, 63-86. http://dx.doi.org/10.1029/166gm06.
[55] Spandler, C.; Pirard, C. Element recycling from subducting slabs to arc crust: A review. Lithos. 2013, 170-171, 208-223.
[56] Kelemen, P.B.; Johnson, K.T.M.; Kinzler, R.J.; Irving, A.J. High-field-strength element depletions in arc basalts due to mantle–magma interaction. Nature. 1990, 345, 1990, 521–524.
[57] Kay, R.W.; Mahlburg Kay, S. Delamination and delamination magmatism. Tectonophysics. 1993, 219 (1–3), 177-189.

[58] Jagoutz, O.; Schmidt, M.W. The composition of the foundered complement to the continental crust and a re-evaluation of fluxes in arcs. Earth and Planetary Sci. Letters, 2013, 371, 177-190.
[59] Halliday, A.N.; Lee, D.C.; Tommasini, S.; Davies, G.R.; Paslick, C.R.; Fitton, J.G.; James, D.E. Incompatible trace elements in OIB and MORB and source enrichment in the sub-oceanic mantle. Earth and Planetary Sci. Letters, 1995, 133(3-4), 379-395.
[60] Tukey, J.W. Exploratory Data Analysis. Addison-Wesley Publishing Company, Massachusett, Reading. 1997.
[61] El-Ramly, M.F.; Ivanov, S.S.; Kochin, G.C. The occurrence of gold in the Eastern Desert of Egypt. Studies on some mineral deposits of Egypt, Part I, Sec A, Metallic Minerals. Geol. Surv., Egypt. 1970, 53-63
[62] Taylor, S.R., McLennan, S.M. The geochemical evolution of the continental crust. Rev. Geophysics. 1995, 33(2), 241-265.
[63] Irvine, T.N.; Baragar, W.R.A. A guide to the chemical classification of the common volcanic rocks. Cana. J. Earth Sci. 1971, 8(5), 523-548.
[64] Maniar, P.D.; Piccoli, P.M. Tectonic discrimination of granitoids. Geol. Soc. Am. Bull. 1989, 101: 636–643.
[65] Boynton, W.V. Geochemistry of Rare Earth Elements: Meteorite Studies. In: Henderson, P., (Ed.), Rare Earth Element Geochemistry, Elsevier, New York, 1984, 63-114.